PNAS RESEARCH ARTICLE | PHYSICS

Field-tuned ferroquadrupolar quantum phase transition in the insulator $TmVO_4$

Pierre Massat[a,1], Jiajia Wen[b], Jack M. Jiang[a,b], Alexander T. Hristov[c], Yaohua Liu[d,e], Rebecca W. Smaha[b,f], Robert S. Feigelson[g], Young S. Lee[a,b], Rafael M. Fernandes[h], and Ian R. Fisher[a,1]

Edited by Zachary Fisk, University of California, Irvine, CA; received November 1, 2021; accepted April 13, 2022

We report results of low-temperature heat-capacity, magnetocaloric-effect, and neutron-diffraction measurements of $TmVO_4$, an insulator that undergoes a continuous ferroquadrupolar phase transition associated with local partially filled $4f$ orbitals of the thulium (Tm^{3+}) ions. The ferroquadrupolar transition, a realization of Ising nematicity, can be tuned to a quantum critical point by using a magnetic field oriented along the c axis of the tetragonal crystal lattice, which acts as an effective transverse field for the Ising-nematic order. In small magnetic fields, the thermal phase transition can be well described by using a semiclassical mean-field treatment of the transverse-field Ising model. However, in higher magnetic fields, closer to the field-tuned quantum phase transition, subtle deviations from this semiclassical behavior are observed, which are consistent with expectations of quantum fluctuations. Although the phase transition is driven by the local $4f$ degrees of freedom, the crystal lattice still plays a crucial role, both in terms of mediating the interactions between the local quadrupoles and in determining the critical scaling exponents, even though the phase transition itself can be described via mean field. In particular, bilinear coupling of the nematic order parameter to acoustic phonons changes the spatial and temporal fluctuations of the former in a fundamental way, resulting in different critical behavior of the nematic transverse-field Ising model, as compared to the usual case of the magnetic transverse-field Ising model. Our results establish $TmVO_4$ as a model material and electronic nematicity as a paradigmatic example for quantum criticality in insulators.

electronic nematicity | quantum criticality | neutron diffraction | specific heat | magnetocaloric effect

Significance

The behavior of metals close to an electronic nematic quantum critical point (QCP) is not well understood. Here, we study the simpler case of an insulator that undergoes a ferroquadrupolar phase transition, which is a specific realization of Ising-nematic order. The ferroquadrupolar transition can be tuned continuously toward a QCP via application of a magnetic field. We find that close to the QCP, the phase boundary deviates from semiclassical predictions, consistent with expectations of quantum fluctuations. The observed power-law dependence is different from that of magnetic Ising systems due to coupling of order-parameter fluctuations to the crystal-lattice fluctuations (phonons). These results provide a well-understood starting point to approach more complex cases of nematic quantum criticality in metallic and disordered materials.

Several experimental and theoretical studies indicate a possible close association between nematic quantum criticality, non-Fermi-liquid behavior, and the occurrence of superconductivity (see, for example, refs. 1–7 and references therein). This is, however, a complicated problem to study, in large part because it is not clear how well the current materials of interest map onto the effective models that are studied theoretically. For instance, iron-based superconductors, which display an unambiguous nematic phase, usually display a closely related antiferromagnetic state as well (8). Furthermore, chemical substitution is often used as the nonthermal control parameter that tunes candidate materials across the putative nematic quantum critical point (QCP). This can be problematic since chemical composition is not a continuous variable, induces quenched disorder, and can affect multiple terms in the effective Hamiltonian in poorly understood and poorly controlled ways. All of these factors motivate development of simpler model systems, for which key terms in the underlying Hamiltonian are well-understood and well-controlled and for which a nematic quantum phase transition (QPT) can be driven in a continuous fashion in situ without the need for chemical substitution. Here, we consider the simplest case of a nematic QCP in an insulator, for which: 1) the nematic degrees of freedom are provided by local atomic orbitals, 2) the electron-hole excitations are gapped, and 3) the QCP can be traversed by application of a magnetic field.

Ferroquadrupolar (FQ) order of local $4f$ orbitals, in which each $4f$ orbital spontaneously acquires an electric quadrupole moment with the same orientation below a critical temperature T_Q, is a specific realization of electronic nematic order (9, 10). Bilinear coupling between the local quadrupole moments and static and dynamic lattice distortions with the same symmetry provides an effective interaction between the local quadrupoles. Under certain conditions, this interaction can then drive a cooperative phase transition to an FQ-ordered state. The FQ ordering is necessarily accompanied by a structural distortion at the same critical temperature T_Q—this is the essence of the cooperative Jahn–Teller effect (11, 12). For the case corresponding to a tetragonal-to-orthorhombic phase transition, the FQ/nematic order parameter has an Ising character, and there are no cubic invariants in the free energy, so the phase transition can be continuous. In the absence of disorder, one anticipates mean-field behavior for the thermal phase transition

Author contributions: P.M., J.W., J.M.J., A.T.H., Y.L., R.W.S., Y.S.L., R.M.F., and I.R.F. designed research; P.M., J.W., J.M.J., A.T.H., R.W.S., and R.S.F. performed research; P.M. and R.S.F. contributed new reagents/analytic tools; P.M., J.W., J.M.J., A.T.H., R.W.S., and R.S.F. analyzed data; and P.M., J.W., J.M.J., A.T.H., Y.L., R.W.S., R.S.F., Y.S.L., R.M.F., and I.R.F. wrote the paper.

The authors declare no competing interest.

This article is a PNAS Direct Submission.

[1]To whom correspondence may be addressed. Email: pmassat@stanford.edu or irfisher@stanford.edu.

This article contains supporting information online at https://www.pnas.org/lookup/suppl/doi:10.1073/pnas.2119942119/-/DCSupplemental.

Published July 5, 2022.

since the upper critical dimension (d_c^+) for the Ising-nematic model with strain-mediated long-range interactions is two (13, 14). Under certain conditions, met for $TmVO_4$, a formal mapping to the Transverse Field Ising Model (TFIM) can be made, in which a magnetic field applied along the crystalline c axis acts as an effective transverse field for the local quadrupoles, effectively suppressing the quadrupole order (9). What makes this system fundamentally different from the usual magnetic realization of the TFIM [as in, e.g., $LiHoF_4$ (15, 16)] is the aforementioned bilinear coupling between the FQ order parameter and lattice deformations with the same symmetry. This coupling not only renders the thermal phase-transition mean field (by changing d_c^+ from four to two, as noted above), but, as we will show, also determines the critical behavior associated with the field-tuned QCP (14).

The title material, $TmVO_4$, is an insulator. It undergoes a continuous FQ phase transition at 2.2 K, with all the action driven by the local partially filled $4f$ orbital of the Tm ion. Magnetic interactions are weaker than the quadrupole–quadrupole interactions, and no magnetic order is observed. Material analogs that lack the partially filled $4f$ orbital, such as YVO_4, do not undergo a similar phase transition, demonstrating that the crystal lattice is perfectly stable in the absence of the Jahn–Teller effect driven by local quadrupolar moments (*SI Appendix*). At high temperatures, the material has tetragonal symmetry, with the Tm ions occupying a unique crystallographic site with D_{2d} symmetry (Fig. 1, *Inset*). The ground state of the Tm ion in the presence of the crystal electric field (CEF) is a non-Kramers orbital doublet that transforms as the E irreducible representation of the D_{2d} symmetry. It is this degeneracy that drives the FQ phase transition. The first excited CEF state is 54 cm^{-1} (6.7 meV) above the ground-state doublet (17), so at low temperatures, the system can be described in terms of a pseudospin to a very good approximation. Below T_Q, the material develops spontaneous ϵ_{xy} strain, corresponding to a nematic order parameter that transforms as the B_{2g} irreducible representation of the point group of the tetragonal crystal lattice. Thus, the principal axes of the resulting orthorhombic state are rotated by 45° with respect to those of the high-temperature tetragonal structure.

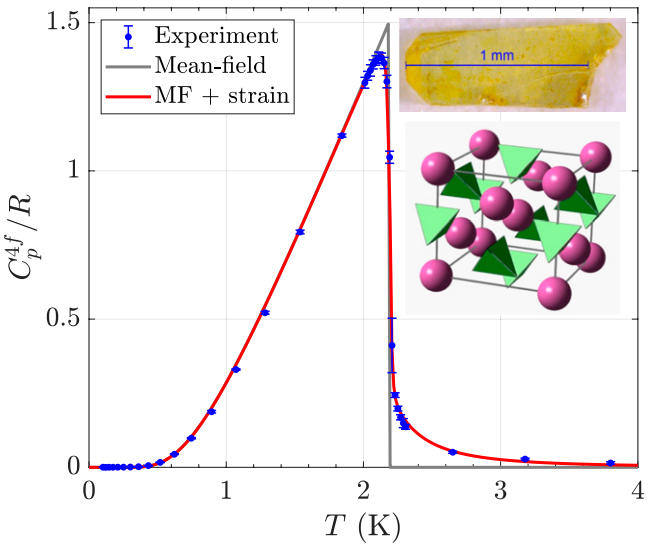

Fig. 1. Temperature dependence of the heat capacity of $TmVO_4$ in zero magnetic field, illustrating the mean-field character of the phase transition. Data (blue points) are shown after subtraction of the phonon thermal contribution and are normalized to the gas constant R. The gray line shows the mean-field model, for which the only free parameter is the value of T_Q. The red line includes phenomenological parameters to account for broadening of the phase transition at T_Q (modeled here by a small strain of the same symmetry as the order parameter) and the contribution to the heat capacity above T_Q (modeled by a small temperature-independent stress), as described in *SI Appendix*. *Upper Inset* shows an image of the sample on which these zero-field data were measured. To minimize demagnetizing effects, needle-shaped samples were used for measurements close to the field-tuned QCP. *Lower Inset* illustrates the zircon-type crystal structure in the tetragonal phase, with Tm ions represented by purple spheres and VO_4 molecular clusters by green coordination polyhedra. MF, mean field.

This material was extensively studied in the 1970s and 1980s, in part because of the "ideal" mapping to simple pseudospin models of the cooperative Jahn–Teller effect. A series of beautiful measurements established that the zero-field thermal phase transition of $TmVO_4$ is indeed mean-field-like, including measurements of heat capacity (which shows the canonical mean-field "step" seen in Fig. 1) (18), optical absorption (19), Raman spectroscopy (20), ultrasound (21, 22), X-ray diffraction (23), Mössbauer spectroscopy (24), inelastic neutron scattering (25), electron paramagnetic resonance (26), and NMR (27, 28). Indeed, the material was seen as a model system for mean-field thermal phase transitions (12). Similarly, the shape of the phase boundary in the $H-T$ plane appeared to conform to mean-field expectations in the temperature range considered, based on a simple semiclassical solution of the TFIM. In this approach, the quantum dynamics associated with the noncommuting pseudospin operators in the TFIM are neglected, such that the external transverse field and the intrinsic Weiss longitudinal field experienced by the local quadrupoles are simply added in quadrature (29). However, when the material was first investigated, notions of both QPTs and electronic nematic order had yet to be considered in detail in the context of condensed matter. As a result, the physical properties of the system were not followed to low temperatures, proximate to what we would now understand to be a putative FQ QCP. Recent theoretical studies of electronic nematic order, inspired by materials such as the Fe-based superconductors, have underscored the importance of the bilinear coupling of order-parameter fluctuations to lattice deformations with the same symmetry (14, 30, 31). Indeed, as we will show, this coupling profoundly affects the resulting critical behavior that characterizes the continuous mean-field QPT.

In this article, we report results of measurements of $TmVO_4$ that probe the field dependence of the order parameter at low temperatures and the shape of the phase boundary approaching the field-tuned QCP. Far from the QCP, the material is well-described by the semiclassical treatment of the TFIM discussed above, in which dynamics associated with the noncommuting operators is neglected. Closer to the QCP, however, subtle deviations are evident, which we argue arise as a consequence of the quantum fluctuations. We discuss expectations for the associated mean-field QCP. In particular, because the dimensionality d is greater than d_c^+ for both the classical phase transitions and QPTs, we can obtain T_Q as a function of $(H - H_c)$ by computing the Gaussian-fluctuations corrections to the free energy, which are well-controlled in this case. Bilinear coupling of the FQ order parameter to phonon modes with the same symmetry necessarily changes these exponents relative to the case of the magnetic TFIM. Our experimental observations and associated theoretical treatment elevate $TmVO_4$ to the status of a model material system, not only to reveal mean-field behavior at the thermal phase transition in zero field (the primary result from the 1970s), but now also to elucidate the effects of quantum critical fluctuations proximate to the mean-field continuous FQ QPT.

Results

Far from the QCP. The cooperative Jahn–Teller effect in $TmVO_4$ results in a pseudoproper ferroelastic phase transition. Bilinear coupling between the FQ order parameter and the ϵ_{xy}

orthorhombic lattice distortion ensures that the temperature and field dependence of the lattice distortion, measured here via elastic neutron scattering, is the same as that of the local quadrupole moments. The orthorhombicity, defined as $\delta = |a - b| / ((a + b)/2)$, was determined from the splitting of the $(880)_T$ Bragg peak, where the subscript T denotes (hkl) labeling according to the high-temperature tetragonal unit cell, whereas a and b are the lattice parameters in the low-temperature orthorhombic phase. Measurements were performed at a temperature $T = 0.60\,\mathrm{K} \approx 0.27\,T_Q$ as a function of magnetic field H, with the field oriented along the crystalline c axis. Demagnetization effects were modeled by using a finite elements simulation, discussed in greater detail in *SI Appendix*.

As shown in Fig. 2*A*, increasing H results in a continuous suppression of the order parameter for the ferroelastic distortion, with the two Bragg peaks, associated with the two orthorhombic domains, eventually merging into a single peak. Peaks for each value of the magnetic field were fitted by using a standard neutron time-of-flight functional form (32, 33), in order to identify the positions $x_{M,1}$ and $x_{M,2}$ of their maxima, from which the relative distortion was deduced as $2\,|x_{M,1} - x_{M,2}|\,/\,|x_{M,1} + x_{M,2}|$

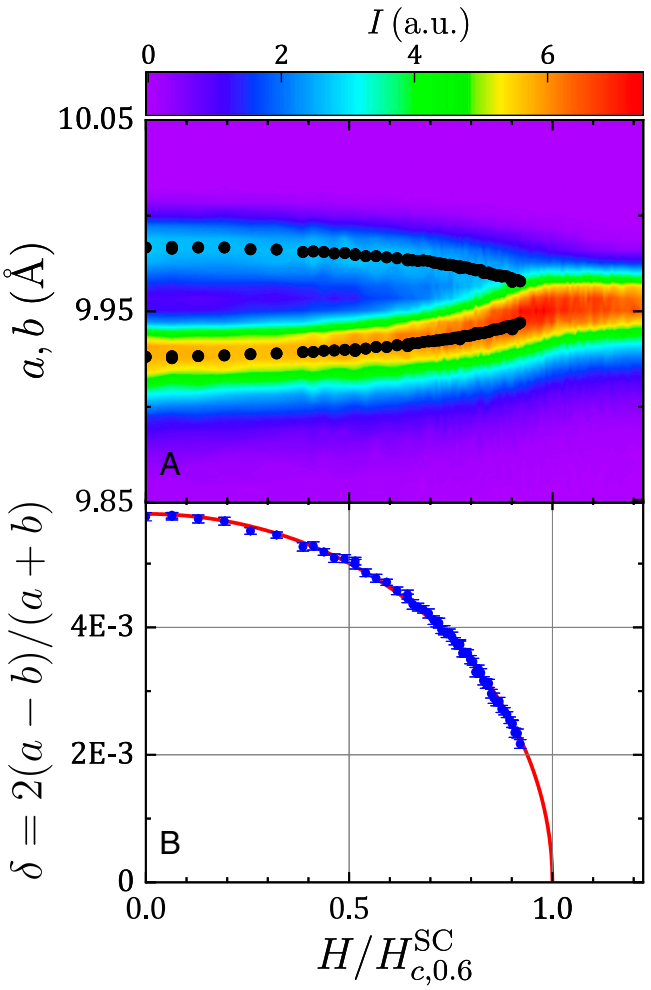

Fig. 2. Field dependence of the lattice parameters *a* and *b* in the orthorhombic phase (*A*) and the orthorhombicity parameter δ at $T = 0.60$ K (*B*). $H^{SC}_{c,0.6}$ is the critical field derived from the semiclassical fit described in Eq. **1**. The color scale in *A* corresponds to detector intensities integrated over the transverse scattering direction. Superimposed are the data points indicating the positions of the peak maxima (black dots). Differences in the intensity of the two peaks are due to differences in the domain population. The orthorhombicity parameter closely follows the semiclassical mean-field solution for the order parameter of the TFIM (red line in *B*). a.u., arbitrary units.

(*SI Appendix*). Its dependence on the magnetic field H, plotted in Fig. 2*B*, closely follows what is expected from semiclassical mean-field treatments of the TFIM, where the transverse (magnetic) and longitudinal (B_{2g} strain) fields add in quadrature (29):

$$\delta(T = 0.6\,\mathrm{K}, H) = \delta_0(0.6\,\mathrm{K}) \cdot \sqrt{1 - \left(\frac{H}{H^{\mathrm{SC}}_{c,0.6}}\right)^2}, \qquad [1]$$

where $\delta_0(0.6\,\mathrm{K})$ is the orthorhombic distortion in the absence of magnetic field, and $H^{SC}_{c,0.6}$ is the critical field at $T = 0.6$ K, derived from this semiclassical fit.

Eq. **1** fits the data very well up to $H/H^{SC}_{c,0.6} \approx 0.92$, with no systematic deviations between the data and the semiclassical mean-field solution discernible within experimental error. For fields above this value, the peak-fitting is not constrained enough to give reliable values due to the instrumental resolution. The semiclassical mean-field fit yields $\delta_0(0.6\,\mathrm{K}) = 5.78(4) \cdot 10^{-3}$, in agreement with previous estimates for the zero-temperature orthorhombicity based on the same semiclassical model (23).

A further test of the extent to which $TmVO_4$ follows semiclassical mean-field expectations as a function of field is provided by the shape of the phase boundary, which is best determined by thermodynamic probes. Heat-capacity measurements were performed in a Helium-3 (He-3) refrigerator down to 0.35 K.

The temperature and field dependence of the heat capacity (data points in Fig. 3*A*) closely agree with the semiclassical mean-field solution of the TFIM (29, 34). In particular, they exhibit three main features as the magnetic field is increased: 1) The step marking the phase transition moves to lower temperatures and is suppressed in magnitude; 2) the data fall onto the same curve below the transition temperature $T_Q(H)$; and 3) the high-temperature tail of a Schottky anomaly is clearly visible above the transition temperature due to splitting of the ground-state doublet induced by the magnetic field.

Rounding of the mean-field step in the heat capacity is evident in Figs. 1 and 3*A*. This effect is attributed to small, unintentional strain of the same symmetry as the order parameter and, for measurements made in magnetic fields, demagnetization effects. In zero field, the upward curvature of the heat capacity for temperatures above T_Q can be accounted for by a small residual stress, which could arise, for example, from freezing of the grease used to hold the sample to the calorimeter platform or possibly even from crystal growth defects. While both sources of strain are likely inhomogeneous, the data can be very well described by treating both by a single uniform parameter (solid red line in Fig. 1). These subtle effects are, of course, still present when the measurements are made in an applied field, but are swamped by the much larger field-induced effects associated with inhomogeneous demagnetization and field-induced splitting above T_Q.

Demagnetizing effects were modeled by using finite element simulations (*SI Appendix*). This resulted in a very good description of the data through T_Q for all fields (solid lines in Fig. 3*A*).* It is worth noting that only the solid (zero field) blue line is an actual fit of the corresponding data, with two free parameters, $T_{Q,0}$, the zero-field transition temperature, and ε, the homogeneous longitudinal field responsible for the rounding of the transition. All other solid lines at finite fields were computed numerically without any free parameters using: 1) the values obtained for $T_{Q,0}$

*The constant stress underlying the phenomenological fit of the high-temperature tail of heat capacity, as shown in Fig. 1, is independent of magnetic field. Since we focus here on the effects of magnetic field on the heat capacity, we do not include this high-temperature contribution in our modelling.

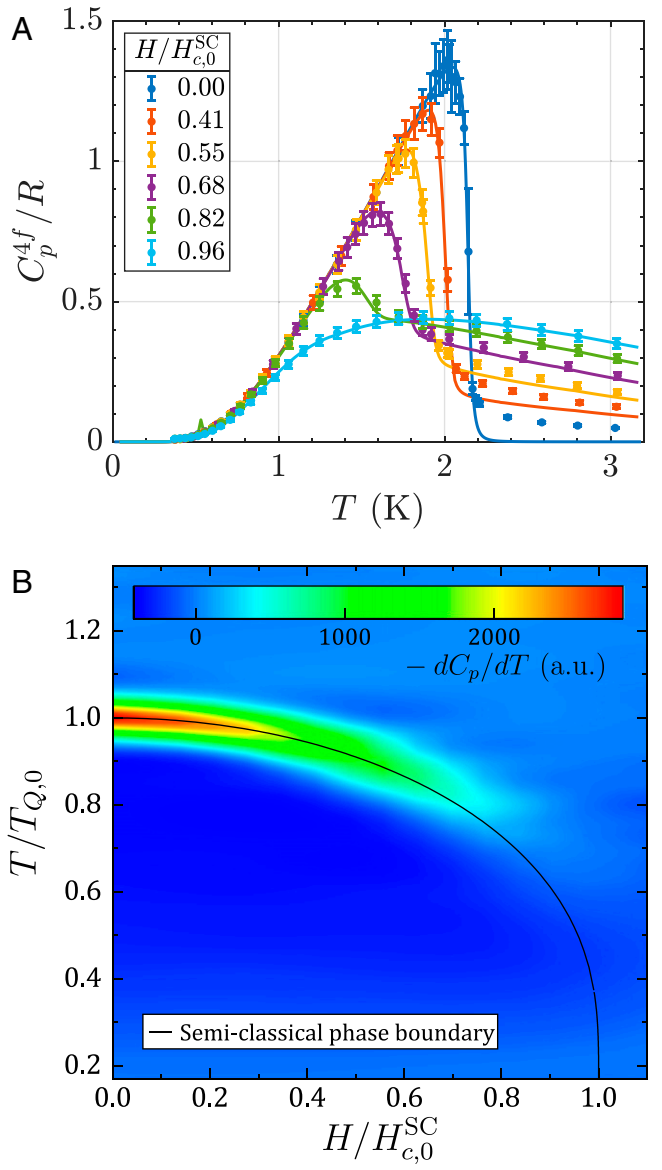

Fig. 3. (*A*) Temperature dependence of the heat capacity of $TmVO_4$ under various values of externally applied magnetic field H, in units of the gas constant R. Symbols: experimental data. Full line at zero field: mean-field fit using the semiclassical TFIM. All other solid lines: mean-field computations of the semiclassical solution of the TFIM, combined with the distributions of magnetic fields inside the sample, as computed by using COMSOL (see *Far from the QCP*). (*B*) Temperature–magnetic-field phase diagram, as obtained from the first derivative of the heat capacity (color map). The black line is the theoretical phase boundary according to the semiclassical mean-field solution of the TFIM. $T_{Q,0}$ is the transition temperature in the absence of magnetic field; $H_{c,0}^{SC}$ is the critical transverse magnetic field at $T = 0$, as extracted from fitting the heat-capacity data with the semiclassical expression for the phase boundary. a.u., arbitrary units.

and ε from the fit of the zero-field data; and 2) the magnetic-field distributions computed in COMSOL.

For magnetic fields up to $\sim 0.9\, H_c(T=0)$, the critical temperature can be readily extracted from the first temperature derivative of the heat-capacity data, dC_p/dT, which is plotted as a color map on the T–H plane in Fig. 3*B*. The same figure also displays the semiclassical mean-field phase boundary (black line), which is described by the following functional form (29):

$$\frac{T_Q(H)}{T_{Q,0}} = \frac{H/H_{c,0}^{SC}}{\operatorname{atanh}\left(H/H_{c,0}^{SC}\right)}, \qquad [2]$$

where $T_{Q,0}$ is the zero-field transition temperature, $H_{c,0}^{SC}$ is the zero-temperature critical field, and atanh is the inverse tanh function. This equation fits the phase boundary obtained from heat-capacity data very well for fields up to $\sim 0.8\, H_{c,0}^{SC}$.

Close to the QCP. The small magnitude of the heat-capacity anomaly for higher fields, combined with the steep shape of the mean-field phase boundary, renders heat-capacity measurements less helpful for determining T_Q closer to the QCP. For this reason, we instead use the Magnetocaloric Effect (MCE).

MCE measurements were made by using the same calorimeter as the heat-capacity measurements in the He-3 fridge and also by using a different calorimeter in a separate dilution refrigerator. Representative data, along with a description of the physical principle of the MCE, can be found in *SI Appendix*. Under quasiadiabatic conditions, to compensate for the release of entropy associated with the quadrupolar degrees of freedom at the FQ transition, the temperature of the sample changes. For each MCE trace, $H_c(T)$ was thus identified as the magnetic-field value at which the second derivative of the field-induced temperature change of the sample $\frac{d^2\Delta T}{dH^2}$ is maximum.

The values of $H_c(T)$ extracted via MCE measurements are plotted in Fig. 4 as green dots with horizontal error bars, along with the transition temperatures $T_Q(H)$ extracted from the heat-capacity data, plotted as blue dots with vertical error bars. The combination of all these data into a single dataset was then fitted on various ranges of magnetic field, using the expression for the phase boundary in the semiclassical description of the TFIM, Eq. **2**. The best fit was obtained when fitting over the range $0 \le H \le 4$ kOe, with an adjusted R^2 of 0.9998 (*SI Appendix*, section S7). The corresponding curve is plotted as a red solid line in Fig. 4. While in the field range between 0 and 4 kOe, the curve goes through all the data points, it overshoots the data for fields larger than 4 kOe, when the QCP is approached.

It is worth noting that this result is not an artifact of data obtained from two different types of measurements, as the heat-capacity data point located at $H = 4.5$ kOe is in agreement with the MCE data. Moreover, both measurements were performed

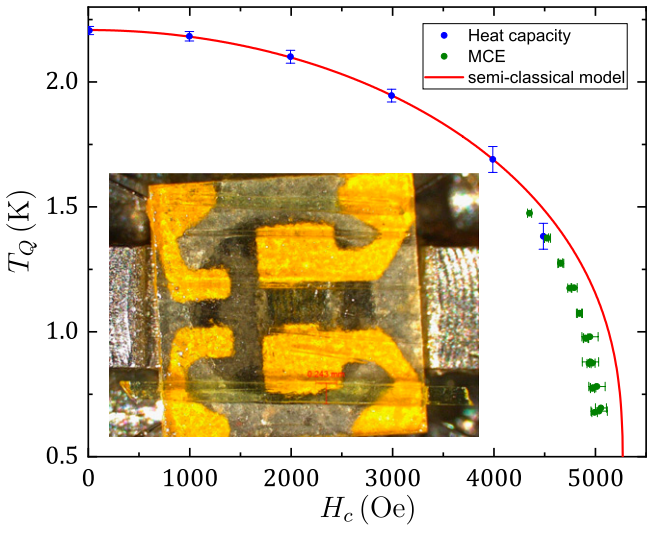

Fig. 4. Experimentally determined phase boundary $T_Q(H)$ extracted from measurements of heat capacity (blue data points with vertical error bars) and magneto-caloric effect (green data points with horizontal error bars). The red line shows the fit of the phase boundary using the semiclassical solution of the TFIM, including data points at or below 4 kOe only (see *Close to the QCP*). *Inset* shows a picture of the sample, made of a collection of needles to minimize demagnetization effects, on the heat-capacity platform.

in a single run using the same setup. Lastly, these results were reproduced on the sample of Fig. 1.

Since the data deviate from the semiclassical mean-field solution of the TFIM, we used a self-consistent Gaussian-fluctuation approach to calculate the expected shape of the phase boundary. This method includes the leading order contribution of the quantum fluctuations to $T_Q(H)$, which should be sufficient since the system is above the upper critical dimension (35). Our model predicts a power-law behavior close to the QCP (below and *SI Appendix*)—i.e., $T_Q \sim \left(H_{c,0}^{\mathrm{PL}} - H_c(T)\right)^{\psi}$, where $H_{c,0}^{\mathrm{PL}}$ denotes the estimated critical field at zero temperature, as determined from the power-law fit. Fitting the data of Fig. 4 with this expression yields $H_{c,0}^{\mathrm{PL}} = 5{,}008(4)$ Oe and $\psi = 0.21(2)$, with a best-fit range $4.5\,\mathrm{kOe} \leq H \leq 5.0\,\mathrm{kOe}$ and an adjusted R^2 of 0.97. The resulting best-fit curve is shown as a red solid line on top of the data (black dots) in the log–log plot of Fig. 5.

We note that the neutron-scattering data shown in Fig. 2 are only able to resolve the orthorhombicity over a regime of field and temperature that predominantly lies outside (and barely overlaps with) the proposed quantum critical regime, where power-law behavior of the critical temperature is observed. This is a consequence of the very steep phase diagram. Nevertheless, if the orthorhombicity could be resolved closer to H_c, this, too, must deviate from the semiclassical model in order to match the observed phase diagram.

Discussion

Power-law behavior of the phase boundary $T_Q \sim \left(H_{c,0}^{\mathrm{PL}} - H_c(T)\right)^{\psi}$ is a characteristic feature of quantum criticality (35). The associated quantum fluctuations, presumably promoted by the applied magnetic field acting as a transverse nematic field (9), suppress the critical temperature below what would be anticipated based solely on the semiclassical solution described above. Significantly, bilinear coupling of the Ising-nematic order parameter to dynamic ϵ_{xy} shear deformations makes this fundamentally different from the magnetic TFIM case, as widely studied, for instance, in $LiHoF_4$ (15, 16). Indeed, as we show below, the QCP is characterized by different scaling exponents.

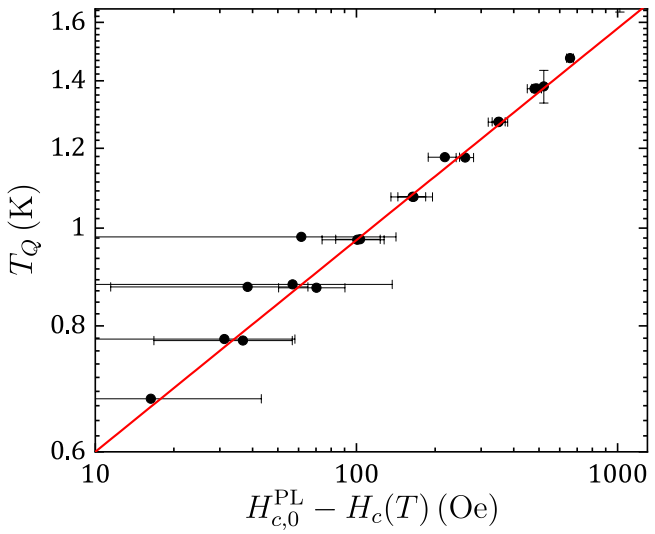

Fig. 5. Log–log plot of the phase boundary $T_Q(H)$. The experimental data (black dots with error bars) were fitted by a power law, $T_Q \sim (H_{c,0}^{\mathrm{PL}} - H_c(T))^{\psi}$. The best fit, plotted as a red solid line, yields $\psi = 0.21(2)$ and $H_{c,0}^{\mathrm{PL}} = 5{,}008(4)$ Oe. The latter value is used as reference for the horizontal axis of the figure.

It is well-established that the thermal phase transition for Ising-nematic order is mean-field-like due to the long-range nematic interaction generated by the coupling to acoustic phonons (13, 14, 36). Because the correlation length only diverges along specific in-plane directions in momentum space (at 45° with respect to the principal axes of the nematic distortion), the upper critical dimension of the problem is reduced from four (for the simple Ising model) to two. Equivalently, the effective dimensionality d of the system increases from three to five due to this coupling—i.e., the material behaves like an Ising system in $d = 5$. Proximate to the QCP, the effective dimensionality increases yet again to $d + z$ (35), where z is the dynamical critical exponent that characterizes temporal fluctuations of the order parameter near the QCP. In other words, since the thermal phase transition for Ising-nematic order in a compressible lattice is mean-field-like, the QCP should also be.

Since mean-field behavior is observed across the entire phase diagram, and the Ginzburg criterion is never violated, a one-loop self-consistent approximation is sufficient to describe how the transition temperature is suppressed to zero by Gaussian quantum fluctuations in an insulator (35). For strong nemato-elastic coupling, appropriate for this system, in which the nematic order only exists because of coupling to the lattice, this calculation results in an exponent that is consistent with the standard scaling relation $\psi = z/(z + d - 2)$ (35) with $d = 5$ (*SI Appendix*). However, since the phase boundary is measured over a range of temperatures and magnetic fields, different exponents can be manifested in different temperature/magnetic-field regimes, corresponding to different values of z, while still belonging to the same mean-field description. To understand why z changes as the QCP is approached, we note that in an insulator, the critical dynamics of a generic bosonic mode is expected to be propagating, resulting in $z = 1$. However, a quantum elastic transition (i.e., arising from the softening of a shear mode) has an exponent $z = 2$ (31, 37). This follows from the fact that the dispersion relation $\omega(q)$ for the soft acoustic phonons (with wave vector along [100] and [010]) at the critical field is only linear for high q values, crossing over to quadratic behavior approaching $q = 0$ due to the vanishing of the sound velocity (38, 39). Consequently, as temperature is decreased and the nematic QCP is approached, a cross-over is anticipated from a regime in which temporal fluctuations are characterized by $z = 1$ to one characterized by $z = 2$. The associated exponent describing the phase boundary in these two regimes is then expected to change from $\psi = 1/4$ ($d = 5$, $z = 1$) at higher temperatures to $\psi = 2/5$ ($d = 5$, $z = 2$) at lower temperatures. The cross-over scale is set not only by the nemato-elastic coupling, which also affects the cross-over from $d = 3$ to $d = 5$, but also by the ratio between the velocities of propagation of sound and of the nematic mode (i.e., collective excitations of the nematic degrees of freedom; *SI Appendix*). As a result, the cross-over scale from $d = 3$ to $d = 5$, associated with spatial fluctuations, does not need to coincide with the cross-over scale from $z = 1$ to $z = 2$ associated with temporal fluctuations.

The observed exponent $\psi = 0.21 \pm 0.02$ is remarkably close to 1/4, the value anticipated for $d = 5$ and $z = 1$. Under the assumption that this apparent power-law behavior originates from critical scaling, we deduce that for the temperature range over which the measurements were performed, $z = 1$. This would be consistent with a small ratio between the velocity of the bare nematic mode (i.e., unrenormalized by interaction with the lattice) and the bare sound velocity—i.e., the purely electronic nematic fluctuations propagate slower than sound does. The fact that the local $4f$ quadrupoles are essentially only coupled via

the lattice supports this assessment. Presumably, extending our measurements to progressively lower temperatures would reveal a cross-over to a regime in which the $z = 2$ exponent is eventually observed. Of course, our observation of a deviation from the semiclassical model is itself not necessarily direct proof that the effect is driven by quantum criticality, but the observation of power-law behavior with an exponent that is consistent with such a scenario is clearly highly suggestive. Additional measurements probing the behavior of various other thermodynamic quantities to lower temperatures in order to test this hypothesis would be highly welcome.

The proposed interpretation of our result in terms of critical scaling near the field-tuned QCP demonstrates the significance of nemato-elastic coupling in Ising-nematic systems. For the simpler case of the magnetic TFIM, the anticipated exponent describing the phase boundary close to the QCP, obtained from the same self-consistent calculation, is $\psi = 1/2$ ($d = 3$, $z = 1$). In that case, the Ising-magnetic order parameter couples only quadratically to longitudinal strain, which is predicted to result in a first-order transition (40, 41). In the Ising-nematic case, however, the effects of a compressible lattice are fundamentally different: Here, the bilinear coupling of the nematic order parameter to shear strain means that the nematic mode inherits some key properties of the critical elasticity of the lattice (31), such as a strong anisotropy of the correlation length, although the phase transition itself remains continuous (13, 14). Our observation of the associated power law proximate to the QCP underscores a key point that applies to metallic nematic systems just as much as for insulators: Sufficiently close to the QCP (where "sufficiently close" could depend on microscopic details for different material systems), coupling to the lattice fundamentally affects the fluctuating order and cannot be neglected (14, 31, 42). More broadly, our results establish the Ising-nematic QPT in insulators such as $TmVO_4$ as a paradigmatic framework to elucidate quantum criticality, which is complementary to, but qualitatively different from, the standard example of an Ising ferromagnet subjected to a transverse magnetic field (43).

Materials and Methods

For heat-capacity and magneto-caloric effect, single crystals of $TmVO_4$ were grown in a flux of $Pb_2V_2O_7$ using 4 mol% of Tm_2O_3, following the methods described in refs. 44 snd 45. Samples were characterized by using heat-capacity measurements and show high quality with a sharp transition at 2.15 (5) K under zero magnetic field (*SI Appendix*). For neutron-scattering measurements, which require bigger single crystals, the samples were grown by using the floating-zone method, as reported in ref. 46. The crystal structure was verified on a flux-grown sample, by collecting single crystal X-ray diffraction data at Beamline 12.2.1 at the Advanced Light Source, Lawrence Berkeley National Laboratory, which confirmed that the tetragonal $I4_1/amd$ symmetry observed at room temperature (47) persists down to at least 100 K (*SI Appendix*). A Crystallographic Information File (CIF) has been deposited in the Cambridge Crystallographic Data Center (CCDC) (accession code 2117139) (48).

Heat-capacity and MCE measurements were performed in vacuum by using the same setup, with magnetic field parallel to the *c* axis of the sample, and without cycling temperature between one type of measurement and the other. Heat-capacity measurements were carried out under constant magnetic field, from 4 K down to base temperature (0.1 K for the dilution refrigerator, 0.35 K for the He-3 cryostat). For MCE measurements, bath temperature was constant, and magnetic field was swept at a constant rate from 0 to 10 kOe (*SI Appendix*).

Elastic neutron-scattering experiments were carried out in a dilution refrigerator at the CORELLI beamline of the Spallation Neutron Source at Oak Ridge National Laboratory. The sample was aligned in the (*HK*0) scattering plane, with the magnetic field applied vertically along the *c* axis. Data were fitted by using a convolution of a pseudo-Voigt function with the Ikeda–Carpenter function, which is common for time-of-flight neutron-scattering experiments (32) (*SI Appendix*).

Modeling of the sample measured under magnetic field was made by using the AC/DC module of the COMSOL software (49).

Data Availability. Figure data have been deposited in text format in the Stanford Digital Repository (https://purl.stanford.edu/yh091zv1831) (50). The crystallographic information file (CIF) reported in the *SI Appendix* of this paper has been deposited in the Inorganic Crystal Structure Database (ICSD), https://icsd.fiz-karlsruhe.de/search (CCDC deposition number 2117139). These data can be obtained free of charge via https://www.ccdc.cam.ac.uk/structures/, or by emailing data_request@ccdc.cam.ac.uk (48).

ACKNOWLEDGMENTS. Heat-capacity and MCE measurements performed at Stanford University were supported by Air Force Office of Scientific Research Award FA9550-20-1-0252. Crystal-growth experiments were supported by the Gordon and Betty Moore Foundation Emergent Phenomena in Quantum Systems Initiative Grant GBMF9068. The neutron-scattering activities were supported by the US Department of Energy (DOE), Office of Science, Basic Energy Sciences, Materials Sciences and Engineering Division, under Contract DE-AC02-76SF00515. A portion of this research used resources at the Spallation Neutron Source (SNS), a DOE Office of Science User Facility operated by the Oak Ridge National Laboratory (ORNL), and resources of the SNS Second Target Station Project. ORNL is managed by UT-Battelle LLC for the DOE's Office of Science, the single largest supporter of basic research in the physical sciences in the United States. A portion of this research used resources of the Advanced Light Source, a US DOE Office of Science User Facility, under Contract DE-AC02-05CH11231. R.W.S. was supported by NSF Graduate Research Fellowship DGE-1656518. Theory work (R.M.F.) was supported by the US DOE, Office of Science, Basic Energy Sciences, Materials Sciences and Engineering Division, under Award DE-SC0020045. We acknowledge helpful discussions with Yuval Gannot, Marcus Garst, Steve Kivelson, and Indranil Paul. This manuscript has been authored by UT-Battelle, LLC, under Contract DE-AC05-00OR22725 with the US DOE. The US government retains and the publisher, by accepting the article for publication, acknowledges that the US government retains a nonexclusive, paid-up, irrevocable, worldwide license to publish or reproduce the published form of this manuscript, or allow others to do so, for US government purposes. The DOE will provide public access to these results of federally sponsored research in accordance with the DOE Public Access Plan (energy.gov/downloads/doe-public-access-plan).

Author affiliations: [a]Department of Applied Physics, Stanford University, Stanford, CA 94305; [b]Stanford Institute for Materials and Energy Sciences, SLAC National Accelerator Laboratory, Menlo Park, CA 94025; [c]Department of Physics, Stanford University, Stanford, CA 94305; [d]Neutron Scattering Division, Oak Ridge National Laboratory, Oak Ridge, TN 37831; [e]Second Target Station, Oak Ridge National Laboratory, Oak Ridge, TN 37831; [f]Department of Chemistry, Stanford University, Stanford, CA 94305; [g]Department of Materials Science and Engineering, Stanford University, Stanford, CA 94305; and [h]School of Physics and Astronomy, University of Minnesota, Minneapolis, MN 55455

1. T. Shibauchi, A. Carrington, Y. Matsuda, A quantum critical point lying beneath the superconducting dome in iron pnictides. *Annu. Rev. Condens. Matter Phys.* **5**, 113–135 (2014).
2. S. Lederer, Y. Schattner, E. Berg, S. A. Kivelson, Enhancement of superconductivity near a nematic quantum critical point. *Phys. Rev. Lett.* **114**, 097001 (2015).
3. M. A. Metlitski, D. F. Mross, S. Sachdev, T. Senthil, Cooper pairing in non-Fermi liquids. *Phys. Rev. B Condens. Matter Mater. Phys.* **91**, 115111 (2015).
4. S. Lederer, Y. Schattner, E. Berg, S. A. Kivelson, Superconductivity and non-Fermi liquid behavior near a nematic quantum critical point. *Proc. Natl. Acad. Sci. U.S.A.* **114**, 4905–4910 (2017).
5. A. Klein, S. Lederer, D. Chowdhury, E. Berg, A. Chubukov, Dynamical susceptibility of a near-critical nonconserved order parameter and quadrupole Raman response in Fe-based superconductors. *Phys. Rev. B* **98**, 041101 (2018).
6. C. G. Wang *et al.*, Electron mass enhancement near a nematic quantum critical point in $NaFe_{1-x}Co_xAs$. *Phys. Rev. Lett.* **121**, 167004 (2018).
7. T. Worasaran *et al.*, Nematic quantum criticality in an Fe-based superconductor revealed by strain-tuning. *Science* **372**, 973–977 (2021).
8. R. M. Fernandes, A. V. Chubukov, J. Schmalian, What drives nematic order in iron-based superconductors? *Nat. Phys.* **10**, 97–104 (2014).
9. A. V. Maharaj *et al.*, Transverse fields to tune an Ising-nematic quantum phase transition. *Proc. Natl. Acad. Sci. U.S.A.* **114**, 13430–13434 (2017).
10. E. W. Rosenberg, J. H. Chu, J. P. C. Ruff, A. T. Hristov, I. R. Fisher, Divergence of the quadrupole-strain susceptibility of the electronic nematic system $YbRu_2Ge_2$. *Proc. Natl. Acad. Sci. U.S.A.* **116**, 7232–7237 (2019).
11. G. A. Gehring, K. A. Gehring, Co-operative Jahn-Teller effects. *Rep. Prog. Phys.* **38**, 1 (1975).

12. R. Melcher, "The anomalous elastic properties of materials undergoing cooperative Jahn-Teller phase transitions" in *Physical Acoustics*, W. P. Mason, R. Thurston, Eds. (Academic Press, New York, 1976), vol. 12, pp. 1–77.
13. U. Karahasanovic, J. Schmalian, Elastic coupling and spin-driven nematicity in iron-based superconductors. *Phys. Rev. B* **93**, 064520 (2016).
14. I. Paul, M. Garst, Lattice effects on nematic quantum criticality in metals. *Phys. Rev. Lett.* **118**, 227601 (2017).
15. D. Bitko, T. F. Rosenbaum, G. Aeppli, Quantum critical behavior for a model magnet. *Phys. Rev. Lett.* **77**, 940–943 (1996).
16. H. M. Rønnow *et al.*, Quantum phase transition of a magnet in a spin bath. *Science* **308**, 389–392 (2005).
17. K. D. Knoll, Absorption and fluorescence spectra of Tm^{3+} in YVO_4 and YPO_4. *Phys. Status Solidi, B Basic Res.* **45**, 553–559 (1971).
18. A. Cooke, S. Swithenby, M. Wells, The properties of thulium vanadate–An example of molecular field behaviour. *Solid State Commun.* **10**, 265–268 (1972).
19. P. J. Becker, M. J. M. Leask, R. N. Tyte, Optical study of the cooperative Jahn-Teller transition in thulium vanadate, $TmVO_4$. *J. Phys. C Solid State Phys.* **5**, 2027 (1972).
20. R. T. Harley, W. Hayes, S. R. P. Smith, Raman scattering investigations of Jahn-Teller induced phase transitions in $TmAsO_4$ and $TmVO_4$. *J. Phys. C Solid State Phys.* **5**, 1501 (1972).
21. R. L. Melcher, E. Pytte, B. A. Scott, Phonon instabilities in $TmVO_4$. *Phys. Rev. Lett.* **31**, 307–310 (1973).
22. R. L. Melcher, "The anomalous elasticity of materials undergoing cooperative Jahn-Teller phase transitions" in *1973 Ultrasonics Symposium* (IEEE, Piscataway, NJ, 1974), pp. 293–298.
23. A. Segmüller, R. Melcher, H. Kinder, X-ray diffraction measurement of the Jahn-Teller distortion in $TmVO_4$. *Solid State Commun.* **15**, 101–104 (1974).
24. B. B. Triplett, N. S. Dixon, P. Boolchand, S. S. Hanna, E. Bucher, Low temperature Mössbauer studies of thulium compounds. *J. Phys. Colloques* **35**, C6-653–C6-657 (1974).
25. J. K. Kjems, W. Hayes, S. H. Smith, Wave-vector dependence of the Jahn-Teller interactions in $TmVO_4$. *Phys. Rev. Lett.* **35**, 1089–1092 (1975).
26. G. Schwab, W. Hillmer, EPR of non-Kramers rare-earth ions in tetragonal crystals. *Phys. Status Solidi B* **70**, 237–244 (1975).
27. B. Bleaney, M. R. Wells, Radiofrequency studies of $TmVO_4$. *Proc. R. Soc. Lond. A Math. Phys. Sci.* **370**, 131–153 (1980).
28. Z. Wang *et al.*, Anisotropic nematic fluctuations above the ferroquadrupolar transition in $TmVO_4$. *Phys. Rev. B* **104**, 205137 (2021).
29. R. B. Stinchcombe, Ising model in a transverse field. I. Basic theory. *J. Phys. C Solid State Phys.* **6**, 2459 (1973).
30. I. Paul, Magnetoelastic quantum fluctuations and phase transitions in the iron superconductors. *Phys. Rev. Lett.* **107**, 047004 (2011).
31. M. Zacharias, I. Paul, M. Garst, Quantum critical elasticity. *Phys. Rev. Lett.* **115**, 025703 (2015).
32. S. Ikeda, J. M. Carpenter, Wide-energy-range, high-resolution measurements of neutron pulse shapes of polyethylene moderators. *Nucl. Instrum. Methods Phys. Res. Sect. A: Accel. Spectrom. Detect. Assoc. Equip.* **239**, 536–544 (1985).
33. J. Rodríguez-Carvajal, Recent advances in magnetic structure determination by neutron powder diffraction. *Physica B* **192**, 55–69 (1993).
34. R. B. Stinchcombe, Thermal and magnetic properties of the transverse Ising model. *J. Phys. C Solid State Phys.* **6**, 2507 (1973).
35. Hv. Löhneysen, A. Rosch, M. Vojta, P. Wölfle, Fermi-liquid instabilities at magnetic quantum phase transitions. *Rev. Mod. Phys.* **79**, 1015–1075 (2007).
36. Y. Qi, C. Xu, Global phase diagram for magnetism and lattice distortion of iron-pnictide materials. *Phys. Rev. B Condens. Matter Mater. Phys.* **80**, 094402 (2009).
37. R. Folk, H. Iro, F. Schwabl, Critical dynamics of elastic phase transitions. *Phys. Rev. B Condens. Matter* **20**, 1229–1244 (1979).
38. F. Weber *et al.*, Soft phonons reveal the nematic correlation length in $Ba(Fe_{0.94}Co_{0.06})_2As_2$. *Phys. Rev. B* **98**, 014516 (2018).
39. A. M. Merritt *et al.*, Nematic correlation length in iron-based superconductors probed by inelastic X-ray scattering. *Phys. Rev. Lett.* **124**, 157001 (2020).
40. A. I. Larkin, S. A. Pikin, Phase transitions of the first order but nearly of the second. *Sov. Phys. JETP* **29**, 891 (1969).
41. D. J. Bergman, B. I. Halperin, Critical behavior of an Ising model on a cubic compressible lattice. *Phys. Rev. B* **13**, 2145–2175 (1976).
42. V. S. de Carvalho, R. M. Fernandes, Resistivity near a nematic quantum critical point: Impact of acoustic phonons. *Phys. Rev. B* **100**, 115103 (2019).
43. S. Sachdev, *Quantum Phase Transitions* (Cambridge University Press, Cambridge, United Kingdom, 2011).
44. R. Feigelson, Flux growth of type RVO_4 rare-earth vanadate crystals. *J. Am. Ceram. Soc.* **51**, 538–539 (1968).
45. S. H. Smith, B. M. Wanklyn, Flux growth of rare earth vanadates and phosphates. *J. Cryst. Growth* **21**, 23–28 (1974).
46. K. Oka, H. Unoki, H. Shibata, H. Eisaki, Crystal growth of rare-earth orthovanadate (RVO_4) by the floating-zone method. *J. Cryst. Growth* **286**, 288–293 (2006).
47. B. C. Chakoumakos, M. M. Abraham, L. A. Boatner, Crystal structure refinements of zircon-type *M*VO4 (M = Sc, Y, Ce, Pr, Nd, Tb, Ho, Er, Tm, Yb, Lu). *J. Solid State Chem.* **109**, 197–202 (1994).
48. R. Smaha, CCDC deposition number 2117139. Inorganic Crystal Structure Database (ICSD) and Cambridge Crystallographic Data Centre (CCDC). https://www.ccdc.cam.ac.uk/structures/. Deposited 20 October 2021.
49. COMSOL Multiphysics (Version 5.5., COMSOL AB, Stockholm, 2020).
50. P. Massat *et al.*, Data for research paper titled "Field-tuned ferroquadrupolar quantum phase transition in the insulator $TmVO_4$." Stanford Digital Repository. https://purl.stanford.edu/yh091zv1831. Accessed 11 February 2022.